Controlling the wetting transitions of nanoparticles on nanopatterned substrates using an electric current

M. Ignacio and O. Pierre-Louis*

Institut Lumière Matière, UMR5306 Université Lyon 1-CNRS, Université de Lyon 69622 Villeurbanne, France

(Received 13 October 2014; revised manuscript received 22 April 2015; published 10 July 2015)

We study the behavior of a nanoparticle under electromigration on a nanopatterned surface. We show that electromigration allows one to control the wetting transitions of the nanoparticle. Suitable surface electromigration conditions to observe these transitions can be achieved with electric currents larger than 1 μA. Using kinetic Monte Carlo simulations and analytical modeling, we determine the phase diagram of the wetting states, showing how wetting multistability is affected by electromigration. In addition, we show that the dynamics of the transitions is controlled by surface diffusion in our simulations, and we provide a quantitative expression for the transition time.

DOI: 10.1103/PhysRevE.92.012406 PACS number(s): 81.10.Aj, 68.55.−a, 66.30.Qa

I. INTRODUCTION

Controlling the adhesion, shape, and positioning of nanoparticles, nanoislands, or quantum dots on various solid substrates is a central issue in nanoscience. One of the main strategies to achieve this goal is to use substrate patterning. In the past decade, many experiments have proposed to deposit [1,2] or grow [3–5] particles on topographical patterns with small aspect ratios, such as surface undulations [6], or large aspect ratios, such as nanopillar forests [3,7–9] and nanopore arrays [10,11].

When they are successful, these strategies provide some control on the nanoparticles position and properties. However, the resulting configuration is static, and it is in general difficult to change the ordering, positioning, or shape after the formation process. Hence, nanoparticles on surfaces are often seen as morphologically static arrays in which one could only change internal degrees of freedom such as the magnetization or the charge using external fields. Here, using kinetic Monte Carlo simulations complemented with analytical models, we show that one can also control the particle shape and its contact with the substrate using an electric current.

We focus on the morphological changes related to wetting multistability, i.e., the possibility for two or more states to coexist in the same physical conditions. This is one of the main specificities of particles on high aspect ratio nanopatterns [12,13]. Indeed, there are three types of wetting states for nanoparticles on nanopatterned surfaces. They are named after the equivalent liquid-wetting states [14]: (i) the Wenzel (W) state, where the particle is in contact with the substrate surface everywhere in the nanopattern; (ii) the Cassie-Baxter (CB) state, where the gaps within the pattern are empty; (iii) the imbibition state, where the particle collapses completely in the nanopattern, thereby leading to the formation of an imbibition film.

Here, we discuss the transitions between CB and W states (Some additional discussions including the imbibition state are provided in Appendix A). Many experimental observations of CB and W states for nanoparticles have been reported in the literature, e.g., SiGe quantum dots trapped in ring-shape nanotrenches [15], GaAs/Si(100) nanopillars [3], GaN/Si(100) nanopillars [7], GaN/3C-SiC/Si nanopillars [8], Ge/Si(001) nanopillars [9], and GaN/Si nanoporous substrates [10,11]. However, to our knowledge, the transitions between these states have never been observed.

II. KINETIC MONTE CARLO MODEL

Let us assume that an electric current induces the migration of surface atoms. In order to implement the behavior of particles in the presence of a surface electromigration force, we use a 3D kinetic Monte Carlo (KMC) model similar to that of Refs. [12,13,16], extended to account for a migration force **F** following Refs. [17,18]. Atoms are placed on a cubic lattice with a lattice parameter equal to a. Each site can be occupied by a particle atom, a substrate atom, or can remain empty. Substrate atoms are frozen and do not move. We implement surface diffusion along the nanoparticle surface via the hopping of surface atoms. We restrict the motion of atoms to nearest-neighbor hops. In order to only allow for diffusion for atoms along the nanocrystal surface, crystal atoms may move to positions where they have at least one other atom from the particle in the nearest-neighbor (NN) or next-nearest-neighbor (NNN) positions. The hopping rates read

$$\nu = \nu_0 \mathrm{e}^{-(E_J+E_M)/k_BT}. \quad (1)$$

The first contribution to the energy barrier E_J accounts for the breaking of bonds between an atom and its neighbors due to the detachment from its initial position during the hop. We define $E_J = \sum_i n_i J_i$, where J_i are bond energies. The index $i = 1,2$ corresponds, respectively, to NN and NNN between atoms in the particle, and $i = s1,s2$ correspond, respectively, to NN and NNN between particle atoms and substrate atoms.

The effects of the relative values of different bonds between atoms can be simply summarized in two dimensionless parameters.

First, the ratio ζ of nearest-neighbor and next-nearest-neighbor bond energies controls the anisotropic equilibrium shape of the nanocrystal. When $\zeta = 0$, the equilibrium shape is a cube with (100) facets only. A larger ζ leads to the appearance of (111) and (110) facets. If we had aimed at the quantitative comparison of our results with one specific system, the value of

*olivier.pierre-louis@univ-lyon1.fr

ζ would have been chosen to reproduce the equilibrium shape of this system. However, in the following we do not wish to reproduce a specific system, and we therefore use a small ζ to simplify the analysis of the geometry. Moreover, in order to observe fast enough morphological changes, we also want to keep (110) and (111) facets, which are sources of adatoms. Thus, we use $\zeta = 0.2$ in all simulations.

The second parameter $\chi = J_{s1}/J_1$ is the ratio between nearest-neighbor bonds within the particle and nearest-neighbor bonds between the particle and the substrate. In the limit of low temperatures, which correspond to our simulations, one has [12] $\chi = (\gamma_{AV} + \gamma_{SV} - \gamma_{SA})/2\gamma_{SA}$, where the γ are surface free energies and *A, S, V* indicate, respectively, the particle, the substrate, and the vacuum. The parameter χ, called the wettability, describes the wetting properties of the particle on the substrate. If the particle was isotropic like a liquid drop, χ would simply be related to the wetting contact angle via the relation $\chi = (1 + \cos\theta)/2$. In order to use χ to describe our anisotropic solid-state system, we choose arbitrarily the (100) orientation as the reference orientation for surface energies γ. In general, when χ increases, the particle has the tendency to spread more and more on the substrate, and the equilibrium shape on a flat substrate becomes thinner and wider. As $\chi \to 1$ the particle forms a film: this is the wetting transition. We work in the regime of partial wetting with $0 < \chi < 1$. The value of χ has been extracted from experimental observations of the equilibrium crystal shape in various systems, e.g., $\chi = 0.65$ for Si(100) on amorphous SiO_2 (SOI system) [19–21], $\chi = 0.35$ for Pt(111) on yttria-stabilized ZrO_2 [22], $\chi = 0.31$ for Pt(111) on Al_2O_3 [23], and $\chi = 0.26$ for Pt(111) on Si_3N_4 [22].

The second contribution to the energy barrier, E_M, is caused by electromigration. Following Refs. [17,18], one has $E_M = \mathbf{F} \cdot \delta\mathbf{r}$, where $\mathbf{F}$ is the migration force, and $\delta\mathbf{r}$ is the displacement of the adatom from its equilibrium position to the position of the barrier. We also simplify the analysis by assuming that the migration force is constant and along the z axis orthogonal to the average substrate orientation. This amounts to neglecting the possible deflections of the electric current due to the particle and the substrate, but we keep the main ingredient: the existence of an average force directed along the current.

We use periodic boundary conditions in the x, y directions parallel to the average substrate orientation. Particles extend through the whole system size along the x direction but are never in contact with their periodic images along y. In the z direction, the particles cannot hop to heights larger than $z_{\max}$. The value of $z_{\max}$ is chosen to be large enough so that nanoparticles never reach it during the dynamics.

III. PHASE DIAGRAM OF A NANOPARTICLE PARTICLE ON NANOTRENCHES UNDER AN ELECTRIC CURRENT

We choose a specific substrate geometry with a periodic array of parallel nanotrenches where both the CB to W and the W to CB transitions are possible, while this latter transition is usually difficult to obtain on pillars due to pinning effects. This reversibility of the transition has been confirmed both using KMC simulations with nanoparticles on nano-trenches [12] and with electrowetting experiments of water droplets on Teflon-covered microscale trenches [24].

We assume that the trenches exhibit a square section and that the island is periodic in the direction perpendicular to the trenches. The critical forces above which W $\to$ CB and CB $\to$ W transitions are observed depend on model parameters. Since the migration force F is constant, it can be written as the gradient of an effective potential energy $-Fz$. Adding this contribution with surface and interface free energies, we obtain a global effective energy. The variation of this global energy with respect to the island shape provides a criterion for stability. A detailed derivation is given in Appendix A. The variation of the shape considered in the stability criteria are inspired by the observation of the transitions in the KMC simulations. Considering the variation of shape depicted in Fig. 2(a1) for the CB $\to$ W transition, we find that this transition is triggered beyond a critical normalized force $\bar{F}_\downarrow$ obeying

$$(1-2\chi)\left(2+\frac{\bar{F}_\downarrow}{2}\right)^{1/2} = \frac{\bar{F}_\downarrow}{4v^{1/2}}(2-\chi)^{1/2}, \tag{2}$$

where we have introduced the normalized force,

$$\bar{F} = \frac{FN}{\gamma_{100}\lambda}, \tag{3}$$

and the reduced volume,

$$v = \frac{N\Omega}{\lambda^3}. \tag{4}$$

Here, $\Omega = a^3$ is the atomic volume, λ describes the typical scale of the patterns, γ_{100} is the free energy of the (100) facet, N is the number of atoms in the particle, and the force amplitude F is chosen to be positive for downward migration. For the reverse W $\to$ CB transition, following the shape variation depicted in Fig. 2(a2), the critical force $\bar{F}_\uparrow$ is found to obey

$$(1-3\chi)\left(2-\frac{\bar{F}_\uparrow}{2}\right)^{1/2} = \frac{1}{2v^{1/2}}\left(1-\frac{\bar{F}_\uparrow}{2}\right)\left(3-4\chi+\frac{\bar{F}_\uparrow}{32v}\right)^{1/2}. \tag{5}$$

In the limit $\bar{F} \to 0$, we recover the known results describing stability in the absence of migration force [12], with critical wettabilities

$$\chi_{\downarrow 0} = 1/2, \tag{6}$$

$$\chi_{\uparrow 0} = 1/3 - [1 + (1+30v)^{1/2}]/(36v), \tag{7}$$

for the CB $\to$ W and W $\to$ CB transitions, respectively.

The stability thresholds obtained from KMC simulation are plotted in Fig. 2(b). They are in good agreement with the predictions, Eqs. (2) and (5). As a remark, it is actually difficult to obtain accurate thresholds from the simulations because the dynamics is very slow near the transitions. This slowing down of the dynamics will be discussed in the next section. In addition, differences between the predictions and the analytical results may originate from our approximations: (i) we neglect the (110) and (111) facets in Eqs. (2) and (5), and KMC simulations are performed with $\zeta = 0.2$. The influence of a nonvanishing ζ on the equilibrium shape of a crystal on nanotrenches was discussed quantitatively in Ref.

[12]. (ii) Thermal fluctuations are also neglected, both for their influence on the values of surface free energies and for their possible role to help passing over energy barriers. The effect of temperature on the facet free energies is negligible at the temperature $k_BT = 0.5J_1$ used in the simulations, as discussed in Ref. [12]. Moreover, although the fluctuation-driven passage of the system over energy barriers have been observed in Ref. [12], the quantitative prediction of this effect remains a challenge. Globally, and given these limitations, the KMC simulations reported in Fig. 2(b) are in good agreement with the transition lines discussed above.

The distance between the two transition lines in Fig. 2(b) indicates the presence of hysteresis, i.e., the transition will not occur at the same value of the force F for increasing forces, or for decreasing forces. We see in Fig. 2(b) that, in the intermediate range $\chi_{\downarrow 0} < \chi < \chi_{\uparrow 0}$, the particle is stable in the CB and W states, and one can switch from one state to the other using the migration force. Using numbers discussed above for χ, we find that this condition can be obtained for Pt(111) on yttria-stabilized ZrO_2 [22], or Al_2O_3 [23], but not for Si(100) on amorphous SiO_2 [19–21], where χ is too large. For larger values of $\chi > \chi_{\uparrow 0}$, the particle spontaneously comes back to the W state in the absence of migration but can be lifted to a CB state using upward migration. In the opposite regime $\chi < \chi_{\downarrow 0}$, the particle spontaneously relaxes to the CB state without migration, but can be collapsed to the W state in the presence of downward migration.

Using these results, it is possible to obtain a W → CB → W cycle in the intermediate range $\chi_{\downarrow 0} < \chi < \chi_{\uparrow 0}$. Let us indeed consider a particle placed initially on the top of the pattern in a CB state as in Fig. 1(a). In the absence of migration, the particle is stable in this position. Then, we switch on the migration force in the downward direction with $\bar{F} > \bar{F}_{\downarrow}$. If the force is strong enough, the surface atoms migrate downward,

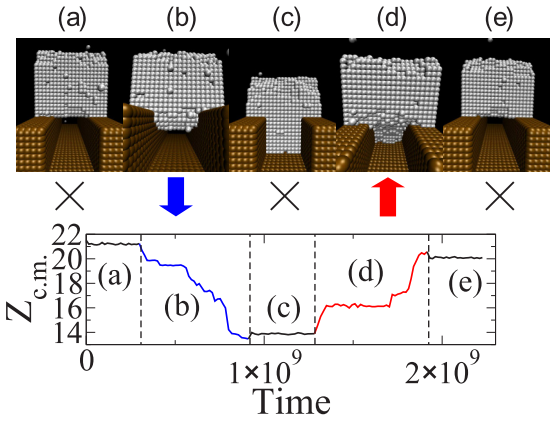

FIG. 1. (Color online) A nanoparticle on a nanopatterned substrate under an electric current can be used as a nanoswitch. The nanoparticle can switch between the Cassie-Baxter state (a, e), and the Wenzel state (b) using electromigration induced by the electric current. The CB → W → CB cycle is obtained using the normalized migration force $\bar{F} = 0$, $\bar{F} = 2.22$, $\bar{F} = 0$, $\bar{F} = -2.22$, and $\bar{F} = 0$. Other simulation parameters: $\zeta = 0.2$, $k_BT = 0.5J_1$, $N = 20^3$, $\chi = 1/3$, and $\lambda = 20a$, where a is the lattice parameter. Lower panel: evolution of the position of the center of mass $Z_{c.m.}$ during the cycle.

leading to a transition to the W state in Fig. 1(b). We then switch off the migration force. The particle is stable in the W state, as shown in Fig. 1(c). A strong enough migration force with $|\bar{F}| > |\bar{F}_{\uparrow}|$ is then turned on in the upward direction. The particle comes back to the CB state; see Fig. 1(d). Once again, and as shown in Fig. 1(e), if the force is switched off, the particle stays in the CB state. We conclude that the system behaves like an addressable bistable nanoscale switch.

IV. TRANSITION DYNAMICS

Finally, we will discuss the dynamics of the transitions. An order of magnitude of the transition time can indeed be obtained from a simple analysis. Let us consider the evolution of a lengthscale ℓ describing the size of the island. The shape evolves due to the migration of adatoms on the lateral facets, creating a total mass flux J. On the one hand, the gradient of chemical potential on the particle surface under the action of the migration force is $\sim F/k_BT$. As a consequence, the total mass flux is $J \sim \ell D C_{\rm eq}(F/k_BT)$, where D and $C_{\rm eq}$ are the adatom diffusion constant and equilibrium concentration on the facets, respectively. On the other hand, mass conservation imposes that $J \sim dN/dt \sim d(\ell^3/\Omega)/dt$, where $N = \ell^3/\Omega$ is the number of atoms of the island, and Ω is the atomic volume. Combining the two expressions of J, one finds $d\ell/dt \sim DC_{\rm eq}F/(\ell k_BT)$. Since the island is displaced by a distance $\sim\lambda$ during collapse, the total transition time is

$$\mathcal{T} \sim \ell\lambda k_BT/(\Omega D C_{\rm eq}|F|). \tag{8}$$

The order of magnitude provided by this expression is in agreement with the simulation results presented in Fig. 2(c). Indeed, since [16] $DC_{\rm eq} = 2 \times 10^{-4}\nu_0$, Eq. (8) predicts $\mathcal{T}_c \sim 8 \times 10^8 \nu_0^{-1}/\bar{F}$. In the KMC simulations presented in Fig. 2(c), both transitions CB → W and W → CB are consistent with a form $\mathcal{T} \sim A/(\bar{F} - \bar{F}_c)$ with $\bar{F}_c \sim 1$ and $A \sim 10^8\nu_0^{-1}$. Here the term $\bar{F}_c$ accounts for the wetting effects, which lead to a finite threshold for the transitions, as obtained in Eqs. (2) and (5). Modeling more precisely the diffusion of mobile adatoms on the lateral facets of the island biased by the migration force, we obtain effective dynamics for the CB → W transition. A detailed and lengthy expression is provided in Appendix B for the time $\mathcal{T}_c$ of transition from the CB state to the W state. This expression with no fitting parameter is in good agreement with the KMC simulations, as seen in Fig. 2(c).

V. DISCUSSION

In order to determine the possibility of migration-induced transitions in experiments, we evaluate the order of magnitude of the ratio F/F_c. In the case of metals, the migration force is dominated by the wind force, which originates in the transfer of momentum of conduction electrons to mobile surface adatoms. Previous studies have shown that $F = ZeE$, where Z is an effective valence, e is the electronic charge, and E is the electric field. Assuming a current I distributed homogeneously in the particle of size w along the trenches, and $w_\perp$ perpendicularly to the trenches, we have $E = \rho I/ww_\perp$, where ρ is the resistivity. In addition, transitions are observed for a critical force $F = F_c$, corresponding to the dimensionless

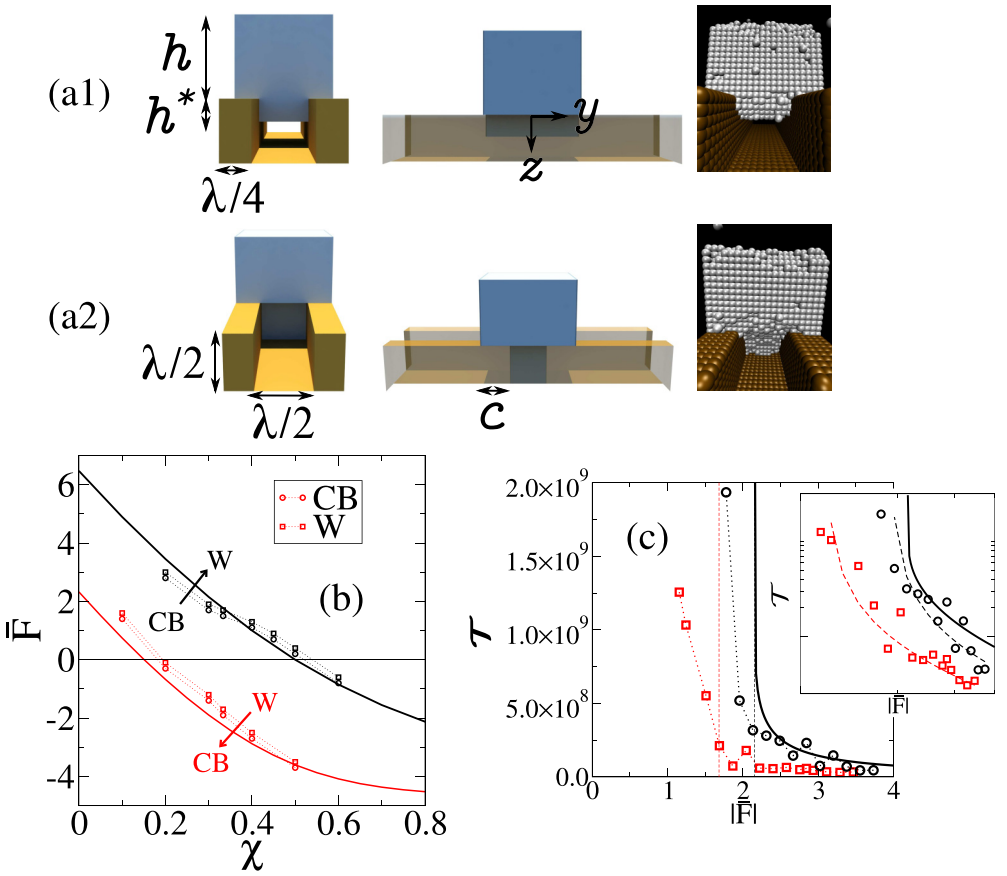

FIG. 2. (Color online) Migration-induced transitions. (a1, a2) Schematics of the intermediate configurations during the CB → W and W → CB transitions, and KMC snapshots. (b) Phase diagram in the presence of migration. The black solid line corresponds to the predicted transition from CB to W from Eq. (2). The prediction for the reverse transition from W to CB is the red solid line, corresponding to Eq. (5). The distance between the two lines indicates the presence of hysteresis. Symbols represent the final state in the KMC simulations: CB (circle) and W (square). The initial state is the W state for the upper curve (W → CB transition) and the CB state for the lower curve (CB → W transition). Other KMC parameters: $\zeta = 0.2$, $k_BT = 0.5J_1$, $N = 20^3$, and $\lambda = 20a$. (c) Transition times $\mathcal{T}_\downarrow$ (black) and $\mathcal{T}_\uparrow$ (red), in units of $1/\nu_0$, as a function of $|\bar{F}|$. KMC simulation results: CB → W (black circle) and W → CB (red squares). The dashed lines report the predicted limit of stability from Eqs. (2) and (5). The solid line is the analytical model for the CB → W transition (described in Appendix A), with no fitting parameter. Other KMC parameters: $\zeta = 0.2$, $\chi = 0.3$, $k_BT = 0.5J_1$, $N = 20^3$, and $\lambda = 20a$. Inset: same data in log scale. The dashed lines correspond to $\mathcal{T}_\downarrow = 0.7 \times 10^8/(\bar{F} - 1.2)$ and $\mathcal{T}_\uparrow = 10^8/(\bar{F} - 1.9)$.

relation $\bar{F} = \bar{F}_c$. We then find

$$\frac{F}{F_c} = \frac{Ze\rho}{\bar{F}_c \Omega \gamma_{100}} I \frac{h}{w_\perp}, \tag{9}$$

where we have used the relation $N = \lambda h w$ corresponding to our geometry. One remarkable consequence of Eq. (9) is that the threshold at fixed current I does not depend on size of the pattern. Furthermore, since we generically expect $w_\perp \sim h$, the dependence on the particle size must be weak. Using typical orders of magnitude $\bar{F}_c \sim 1$, $Z = 10$ to 20 [25–27], $\rho \sim 10^{-8}$ to $10^{-7}\Omega\text{m}^{-1}$, and $\gamma_{100} \sim 0.1$ eVÅ^{-2}, we find that for the largest electric currents usually available in STM or AFM are $I \sim 1\,\mu$A [28,29], $F/F_c \sim 10^{-1} - 10^{-2}$. Hence, the observation of transitions would require higher electric currents, at least 10 μA to reach the threshold.

The timescales of the transition can also be inferred. We use a typical particle size with an aspect ratio around one, i.e., $w \sim w_\perp \sim w \sim \ell$, and Eq. (8) leads to

$$\mathcal{T} \sim \frac{k_BT}{DC_{\text{eq}}} \frac{1}{Ze\rho I} \frac{\ell^3 \lambda}{\Omega}. \tag{10}$$

We assume $DC_{\text{eq}} \sim 10^9$ s^{-1} and $k_BT \sim 0.1$ eV. KMC simulations presented in Figs. 1 and 2 performed with a small particle composed of $N = 20^3 = 8000$ atoms would correspond to a switching time of the order of 1 s, but again with a very high critical current larger than 1 μA.

Globally, the timescales can be changed by several orders of magnitude by changing the migration force, the particle size, or the temperature. But in contrast to the critical force F_c, the transition time at fixed current I is seen to increase with increasing island size ℓ or pattern size λ. Therefore, assuming a fixed current ∼10 μA, the transitions should be observable experimentally in accessible times only for particles up to 100 nm. Observing transitions with larger particles would require higher currents, which are beyond the reach of standard

experimental setups with STM and AFM tips [28,29] and would therefore require a specific device.

Finally, we speculate that another possible strategy to induce migration at the surface could be to use an electron beam. However, there is to our knowledge no experimental observation of electron beam-induced surface migration without damage in the crystal.

In summary, we have shown that, for nanoparticles with significant surface diffusion on frozen substrates, the wetting transitions of a nanoparticle on nanoscale trenches can be controlled by electromigration. Such electric currents could be transmitted from an AFM or STM tip; however, currents larger than those usually available could be necessary. Based on kinetic Monte Carlo simulations and on analytical models, we have obtained a quantitative understanding of the phase diagram and of the transition dynamics.

ACKNOWLEDGMENTS

The authors thank Y. Saito and Maxime Bessette for their contribution to the KMC code, and the referees for important comments. This work is supported by the Agence Nationale de la Recherche (Grant No. ANR-12-BS04-0008 LOTUS).

APPENDIX A: PHASE DIAGRAM FOR A NANOPARTICLE ON NANOTRENCHES IN THE PRESENCE OF A MIGRATION FORCE

In this section, we derive analytical expressions for the transition lines for the CB → W and W → CB transitions. Here, we also consider the CF state, shown in Fig. 3, where CF denotes the capillary-filling state [12], which is the specific imbibition state [12,30] associated with the nanotrench geometry. On the one hand, the W → CF transition must be avoided in order to obtain the two-state nanoswitch discussed in the main text. On the other hand, this transition can be used to obtain a three-state nanoswitch. Below, we obtain a criterion for the W → CF transition.

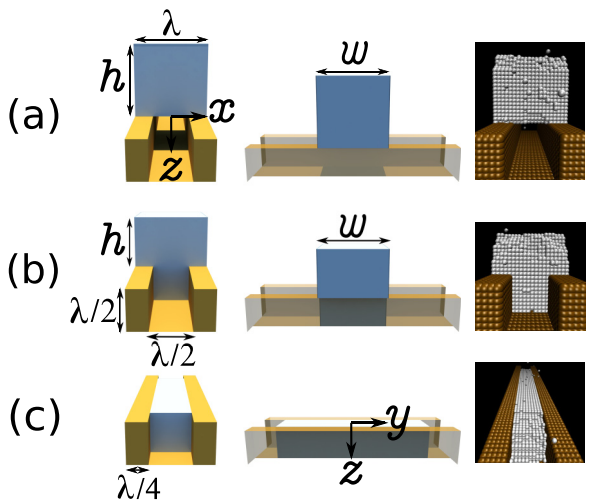

FIG. 3. (Color online) Schematic of the three states: (a) CB, (b) W, (c) CF, and snapshot from KMC simulations.

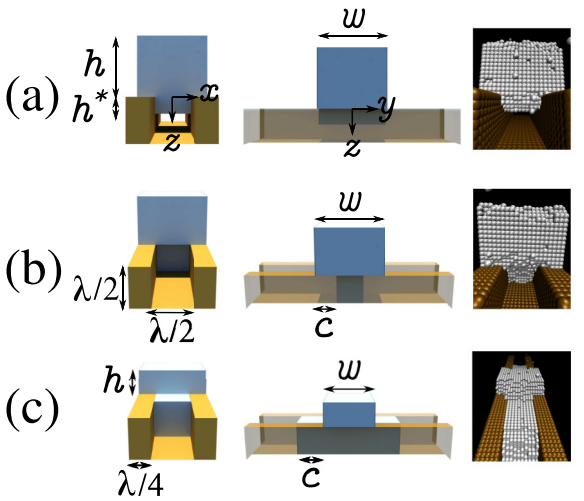

FIG. 4. (Color online) Schematic of the intermediate configurations for the three transitions (a) CB → W, (b) W → CB, and (c) W → CF, and corresponding snapshots from KMC simulations.

In order to simplify the equations, we consider the limit $\zeta \to 0$ where the (110) and (111) facets can be neglected. The crystal then exhibits (100) facets only.

1. CB → W transition

First, let us consider the CB → W transition. The geometrical parameters are shown in Fig. 4(a). As discussed in the main text, the intermediate geometry is inspired by the observation of KMC simulations.

A simple way to account for the migration force is to consider and effective free energy $E - F\int_V dV(z/a^3)$, where E is the surface and interface free energy, the migration force F is positive when it points downward.

The effective free energy during the CB → W transition is parametrized by the length h^* and reads

$$\frac{E_{\mathrm{CB}\to\mathrm{W}}}{\gamma_{\mathrm{av}}} = 2h\lambda + \frac{3}{2}w\lambda + h^*\lambda + (1-2\chi)\left(\frac{\lambda}{2}w + 2wh^*\right) - \frac{F}{\gamma_{\mathrm{av}}a^3}\left(\frac{\lambda w h^{*2}}{4} - \frac{\lambda w h^2}{2}\right). \tag{A1}$$

Using mass conservation

$$V = \lambda w h + \frac{\lambda}{2}wh^*, \tag{A2}$$

the energy Eq. (A1) is rewritten as

$$\frac{E_{\mathrm{CB}\to\mathrm{W}}}{\gamma_{\mathrm{av}}} = \frac{2V}{w} + \frac{3}{2}w\lambda + (1-2\chi)\left(\frac{\lambda}{2}w + 2wh^*\right) - \frac{F}{\gamma_{\mathrm{av}}a^3}\left(\frac{\lambda h^* w}{8} - \frac{V^2}{2w\lambda} + \frac{Vh^*}{2}\right). \tag{A3}$$

We now assume that the shape of the island relaxes at scales faster than the transition time. The equilibrium width w_{eq} of the island is then obtained by solving the equation $\partial_w E_{\mathrm{CB}\to\mathrm{W}} = 0$,

$$w_{\mathrm{eq}} = \left(\frac{2V + \frac{FV^2}{2\lambda\gamma_{\mathrm{av}}a^3}}{\frac{3\lambda}{2} + (1-2\chi)\left(2h^* + \frac{\lambda}{2}\right) - \frac{F\lambda h^{*2}}{8\gamma_{\mathrm{av}}a^3}}\right)^{1/2}. \tag{A4}$$

Inserting this expression into Eq. (A3) leads to

$$\frac{E_{\mathrm{CB}\to\mathrm{W}}}{\gamma_{\mathrm{av}}} = 2\left(2V + \frac{FV^2}{2\lambda\gamma_{\mathrm{av}}a^3}\right)^{1/2} \times\left(\frac{3\lambda}{2} + (1-2\chi)\left(\frac{\lambda}{2}+2h^*\right) - \frac{F\lambda h^{*2}}{8\gamma_{\mathrm{av}}a^3}\right)^{1/2} - \frac{FVh^*}{2\gamma_{\mathrm{av}}a^3}. \quad \text{(A5)}$$

Using reduced units $\bar{F} = F\lambda N/(\gamma_{100}\lambda^2)$ and $v = N\Omega/\lambda^3$, the critical force giving the condition of stability of the CB state is given by $\lim_{h^*\to 0}\partial_{h^*}E_{\mathrm{CB}\to\mathrm{W}} = 0$,

$$(1-2\chi)\left(2+\frac{\bar{F}}{2}\right)^{1/2} = \frac{\bar{F}}{4v^{1/2}}(2-\chi)^{1/2}. \quad \text{(A6)}$$

2. W → CB transition

The observation of KMC simulations reveals that the intermediate stage in the W → CB transition is the formation of a tunnel inside the trench, as depicted in Fig. 4(b). The length of the dewetting tunnel is denoted as $c \geqslant 0$ as shown in Fig. 4(b). The energy of the system during this transition is now

$$\frac{E_{\mathrm{W}\to\mathrm{CB}}}{\gamma_{\mathrm{av}}} = 2h\lambda + \lambda w + \frac{\lambda^2}{2} + c\lambda + \lambda(1-2\chi)(2w-3c) + \frac{F}{\gamma_{\mathrm{av}}a^3}\left(\frac{\lambda^3(w-2c)}{16} - \frac{\lambda w h^2}{2}\right). \quad \text{(A7)}$$

Using mass conservation $V = \lambda wh + \frac{\lambda^2}{4}(w-2c)$, we can calculate once again the equilibrium width of the island during the transition,

$$w_{\mathrm{eq}} = \left[\frac{2V + \lambda^2 c - \frac{F}{\gamma_{\mathrm{av}}a^3}\left(\frac{V^2}{2\lambda} + \frac{\lambda^3c^2}{8} + \frac{V\lambda c}{2}\right)}{\lambda(3-4\chi) + \frac{F\lambda^3}{32\gamma_{\mathrm{av}}a^3}}\right]^{1/2}. \quad \text{(A8)}$$

leading to the equilibrium free energy at fixed c

$$\frac{E_{\mathrm{W}\to\mathrm{CB}}}{\gamma_{\mathrm{av}}} = 2\left[2V + \lambda^2 c - \frac{F}{\gamma_{\mathrm{av}}a^3}\left(\frac{V^2}{2\lambda} + \frac{\lambda^3c^2}{8} + \frac{V\lambda c}{2}\right)\right]^{1/2} \times\left[\lambda(3-4\chi) + \frac{F\lambda^3}{32\gamma_{\mathrm{av}}a^3}\right]^{1/2} + 2c\lambda(3\chi-1) + \frac{FV\lambda}{4\gamma_{\mathrm{av}}a^3}. \quad \text{(A9)}$$

The limit of stability of the Wenzel state is obtained for $\lim_{c\to 0}\partial_c E_{\mathrm{W}\to\mathrm{CB}} = 0$ and reads

$$(1-3\chi)\left(2-\frac{\bar{F}}{2}\right)^{1/2} = \frac{1}{2v^{1/2}}\left(1-\frac{\bar{F}}{2}\right)\left(3-4\chi+\frac{\bar{F}}{32v}\right)^{1/2}. \quad \text{(A10)}$$

3. W → CF transition

When χ or F is large, and points downward, the Wenzel state becomes unstable and the particle collapses into the CF state. The intermediate geometries are similar to those observed for the W → CB transition, except that $c > 0$, i.e., instead of a tunnel, we observe a finger invading the trench in the vicinity of the particle, as shown in Fig. 4(c). The free energy in the intermediate stages is now

$$\frac{E_{\mathrm{W}\to\mathrm{CF}}}{\gamma_{\mathrm{av}}} = 2h\lambda + \lambda w + \frac{\lambda^2}{2} + c\lambda + \lambda(1-2\chi)(2w+3c) - \frac{F}{\gamma_{\mathrm{av}}a^3}\left[\frac{\lambda^3(w+2c)}{16} - \frac{\lambda w h^2}{2}\right]. \quad \text{(A11)}$$

Once again, using mass conservation $V = \lambda wh + \frac{\lambda^2}{4}(w+2c)$, we find the equilibrium shape

$$w_{\mathrm{eq}} = \left[\frac{2V - \lambda^2 c - \frac{F}{\gamma_{\mathrm{av}}a^3}\left(-\frac{V^2}{2\lambda} - \frac{\lambda^3c^2}{8} + \frac{V\lambda c}{2}\right)}{\lambda(3-4\chi) - \frac{F\lambda^3}{32\gamma_{\mathrm{av}}a^3}}\right]^{1/2}. \quad \text{(A12)}$$

Then, we obtain the equilibrium free energy at fixed c

$$\frac{E_{\mathrm{W}\to\mathrm{CF}}}{\gamma_{\mathrm{av}}} = 2\left[2V - \lambda^2 c - \frac{F}{\gamma_{\mathrm{av}}a^3}\left(-\frac{V^2}{2\lambda} - \frac{\lambda^3c^2}{8} + \frac{V\lambda c}{2}\right)\right]^{1/2} \times\left[\lambda(3-4\chi) - \frac{F\lambda^3}{32\gamma_{\mathrm{av}}a^3}\right]^{1/2} - 2c\lambda(3\chi-2) - \frac{FV\lambda}{4\gamma_{\mathrm{av}}a^3}. \quad \text{(A13)}$$

The condition of stability $\lim_{c\to 0}\partial_c E_{\mathrm{W}\to\mathrm{CF}} = 0$ gives the threshold of the transition,

$$(2-3\chi)\left(2+\frac{\bar{F}}{2}\right)^{1/2} = \frac{1}{2v^{1/2}}\left(1+\frac{\bar{F}}{2}\right)\left(3-4\chi-\frac{\bar{F}}{32v}\right)^{1/2}. \quad \text{(A14)}$$

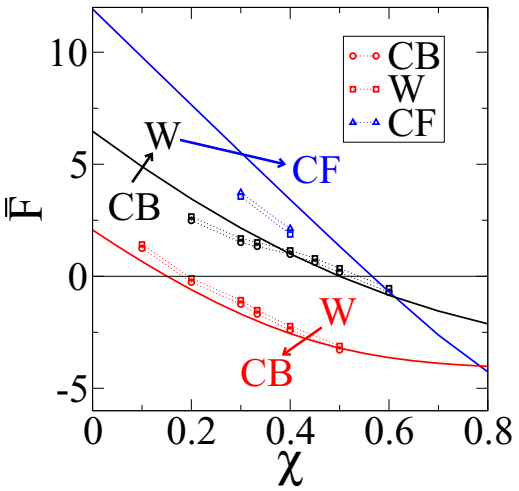

FIG. 5. (Color online) Phase diagram with the CF state. The solid lines report the limits of stability obtained from Eqs. (A6), (A10), and (A14). Symbols indicate the final state in a long KMC simulation: CB (circle), W (square), and CF (triangle). Other KMC parameters: $\zeta = 0.2$, $k_BT = 0.5J_1$, $N = 20^3$, and $\lambda = 20a$.

4. KMC simulations

A comparison between KMC simulations and the analytical predictions is presented in Fig. 5. Given the limitations discussed in the main text, the KMC simulations reported in Fig. 5 are in good agreement with the three transition lines discussed above.

APPENDIX B: DYNAMICS OF THE CB → W TRANSITION

The transition from CB to W state results from the transfer of mass between the top and bottom facets. This mass transfer is mediated by adatoms diffusing on the lateral facets of the island. These adatoms obey a diffusion equation [31,32],

$$\frac{\partial P(z,t)}{\partial t} = -\frac{\partial J(z,t)}{\partial z}, \tag{B1}$$

$$J(z,t) = -D\frac{\partial C(z,t)}{\partial z} + \frac{D}{\xi}C(z,t), \tag{B2}$$

where we have assumed for simplicity that the concentration only depends on the z coordinate. In the following, we use the so-called quasistatic approximation [32], where the adatom diffusion is supposed to be fast, so that one may assume $\partial P(z,t)/\partial t = 0$ in Eq. (B1). The quasistatic approximation relies on the assumption that the adatom concentration profile is not affected by the slow evolution of the island shape. This may be summarized in the separation of scales $D/\partial_t \ell \gg \ell$, where ℓ is the typical size of the island, and Ω is the atomic volume. Since $\partial_t \ell \sim (\Omega/\ell) j$, with a diffusion mass flux $j \sim DC_{\rm eq}/\ell$, where $C_{\rm eq}$ is the equilibrium adatom concentration on facets, the condition of validity of the quasistatic approximation may be rewritten as $\ell \gg \Omega C_{\rm eq}$, which is always verified because $\Omega C_{\rm eq}$ is smaller than an atomic length. As a consequence, the concentration C does not depend explicitly on time and exhibits a simple form,

$$C(z) = A\xi + B\exp(z/\xi), \tag{B3}$$

where A and B are constants. We separate the lateral facets into two zones: (i) $-h < z < 0$, where the facet width is $W = \lambda$, and (ii) $0 < z < h^*$, where the facet width is $W^* = \lambda/2$. At the boundary between the two zones, we assume the continuity of C and J. While the continuity of J strictly follows from mass conservation, the continuity of C is a more delicate assumption, which relies essentially on the fact that the matching region between the two zones is small.

In addition, we assume local equilibrium at $z = h$ and $z = h^*$, leading to two boundary conditions for the concentration: $C(h^*) = C_{\rm eq}\exp[\mu(h^*)/k_BT]$, and $C(-h) = C_{\rm eq}\exp[\mu(-h)/k_BT]$. The local chemical potentials at the top and bottom facets are obtained from the variation of the total energy of the particle:

$$\begin{aligned}\mu(z=-h) &= \frac{\partial E}{\partial h}\frac{\partial h}{\partial N} = \frac{2\Omega\gamma_{\rm av}}{w}\\ \mu(z=h^*) &= \frac{\partial E}{\partial h^*}\frac{\partial h^*}{\partial N} = 2\Omega\gamma_{\rm av}\left(\frac{1}{w}+\frac{2-4\chi}{\lambda}\right),\end{aligned} \tag{B4}$$

leading to $\Delta\mu = \mu(z=h^*) - \mu(z=-h) = -2\Omega\gamma_{\rm av}(2-4\chi)/\lambda$. Note that the z axis is pointing downward.

The boundary conditions lead to a linear system of equations for $A_\pm, B_\pm$. We solve this system in the limit $\xi \gg h, h^*$ and $\mu \ll k_BT$. The time evolution of $h(t)$ and $h^*(t)$ is then given by

$$\begin{aligned}\frac{dh(t)}{dt} &= \frac{-W\Omega}{S}A^- D,\\ \frac{dh^*(t)}{dt} &= \frac{W^*\Omega}{S^*}A^+ D,\end{aligned} \tag{B5}$$

where

$$A^- = W^* C_{\rm eq}\left[\frac{\Delta\mu/k_BT + (h+h^*)/\xi}{Wh^* + W^*h}\right]. \tag{B6}$$

and $A^+ = WA^-/W^*$. In addition, $S = w_{\rm eq}\lambda$ and $S^* = w_{\rm eq}\lambda/2$ denote, respectively, the top and bottom surface facets. Defining

$$\Gamma = C_{\rm eq}\Omega W W^* D\left(\frac{W}{S^*} - \frac{W^*}{S}\right), \tag{B7}$$

$$H^*(t) = h^*(t)\left(W - \frac{W^*S^*}{S}\right) + \frac{W^*V}{S}, \tag{B8}$$

$$a_1 = \frac{2\Gamma}{\xi}\frac{S-S^*}{WS - W^*S^*}, \tag{B9}$$

$$b_1 = 2\Gamma\left\{\frac{\Delta\mu}{k_BT} + \frac{1}{\xi}\left[\frac{-W^*V}{SW - W^*S^*}\left(1-\frac{S^*}{S}\right) + \frac{V}{S}\right]\right\}. \tag{B10}$$

One then has $dH^{*2}/dt = a_1H^* + b_1$. This equation is easily solved, and the total time for the transition from CB state to W state is obtained as

$$\mathcal{T}_\downarrow = \frac{2}{a_1}\left\{H^*(\mathcal{T}_\downarrow) - H^*(0) + \frac{b_1}{a_1}\ln\left[\frac{H^*(0)+\frac{b_1}{a_1}}{H^*(\mathcal{T}_\downarrow)+\frac{b_1}{a_1}}\right]\right\}. \tag{B11}$$

In order to compare this analytical expression of $\mathcal{T}_\downarrow$ to the KMC simulation results, we use the expressions of the physical constants derived in Ref. [12]:

$$D = \nu_0 a^2\exp[-J_1(1+4\zeta)/k_BT], \tag{B12}$$

$$C_{\rm eq} = \exp[-2J_1\beta(1+\zeta)/k_BT], \tag{B13}$$

$$\gamma_{100} = \frac{J_1}{2}(1+4\zeta). \tag{B14}$$

This result is shown in Fig. 2(c) of the main text.

[1] J. Kao, P. Bai, V. P. Chuang, Z. Jiang, P. Ercius, and T. Xu, Nano Lett. **12**, 2610 (2012).
[2] Q. Dai, Y. Chen, C.-C. Liu, C. T. Rettner, B. Holmdahl, S. Gleixner, R. Chung, J. W. Pitera, J. Cheng, and A. Nelson, Langmuir **29**, 3567 (2013).
[3] D. Zubia, S. Zhang, R. Bommena, X. Sun, S. Brueck, and S. Hersee, J. Electron. Mat. **30**, 812 (2001).
[4] V. Repain, G. Baudot, H. Ellmer, and S. Rousset, Europhys. Lett. **58**, 730 (2002).
[5] A. T. N'Diaye, S. Bleikamp, P. J. Feibelman, and T. Michely, Phys. Rev. Lett. **97**, 215501 (2006).
[6] J.-N. Aqua, I. Berbezier, L. Favre, T. Frisch, and A. Ronda, Phys. Rep. **522**, 59 (2013).
[7] S. D. Hersee, X. Y. Sun, X. Wang, and M. N. Fairchild, J. Appl. Phys. **97**, 124308 (2005).
[8] R. Kemper, M. Weinl, C. Mietze, M. Häberlen, T. Schupp, E. Tschumak, J. Lindner, K. Lischka, and D. As, J. Crystal Growth **323**, 84 (2011).
[9] J. Bauer, Y. Yamamoto, P. Zaumseil, O. Fursenko, K. Schulz, G. Kozlowski, M. A. Schubert, T. Schroeder, and B. Tillack, Microelectron. Eng. **97**, 169 (2012).
[10] L. Macht, P. R. Hageman, S. Haffouz, and P. K. Larsen, Appl. Phys. Lett. **87**, 131904 (2005).
[11] K. Y. Zang, Y. D. Wang, S. J. Chua, L. S. Wang, and S. Tripathy, Appl. Phys. Lett. **88**, 141925 (2006).
[12] O. Pierre-Louis and Y. Saito, Europhys. Lett. **86**, 46004 (2009).
[13] M. Ignacio, Y. Saito, P. Smereka, and O. Pierre-Louis, Phys. Rev. Lett. **112**, 146102 (2014).
[14] D. Quéré, Rep. Prog. Phys. **68**, 2495 (2005).
[15] G. Katsaros, J. Tersoff, M. Stoffel, A. Rastelli, P. Acosta-Diaz, G. S. Kar, G. Costantini, O. G. Schmidt, and K. Kern, Phys. Rev. Lett. **101**, 096103 (2008).
[16] M. Ignacio and O. Pierre-Louis, Phys. Rev. B **86**, 235410 (2012).
[17] J. Krug and H. T. Dobbs, Phys. Rev. Lett. **73**, 1947 (1994).
[18] D.-J. Liu and J. D. Weeks, Phys. Rev. B **57**, 14891 (1998).
[19] D. T. Danielson, D. K. Sparacin, J. Michel, and L. C. Kimerling, J. Appl. Phys. **100**, 083507 (2006).
[20] E. Bussmann, F. Cheynis, F. Leroy, P. Müller, and O. Pierre-Louis, New J. Phys. **13**, 043017 (2011).
[21] F. Cheynis, E. Bussmann, F. Leroy, T. Passanante, and P. Müller, Phys. Rev. B **84**, 245439 (2011).
[22] H. Galinski, T. Ryll, P. Elser, J. L. M. Rupp, A. Bieberle-Hütter, and L. J. Gauckler, Phys. Rev. B **82**, 235415 (2010).
[23] M. McLean and E. D. Hondros, J. Mat. Sci. **6**, 19 (1971).
[24] R. J. Vrancken, H. Kusumaatmaja, K. Hermans, A. M. Prenen, O. Pierre-Louis, C. W. M. Bastiaansen, and D. J. Broer, Langmuir **26**, 3335 (2010).
[25] D. N. Bly and P. J. Rous, Phys. Rev. B **53**, 13909 (1996).
[26] P. J. Rous, Phys. Rev. B **59**, 7719 (1999).
[27] E. D. Williams, O. Bondarchuk, C. G. Tao, W. Yan, W. G. Cullen, P. J. Rous, and T. Bole, New J. Phys. **9**, 387 (2007).
[28] B. Xu and N. J. Tao, Science **301**, 1221 (2003).
[29] X. D. Cui, A. Primak, X. Zarate, J. Tomfohr, O. F. Sankey, A. L. Moore, T. A. Moore, D. Gust, G. Harris, and S. M. Lindsay, Science **294**, 571 (2001).
[30] P. Gaillard, Y. Saito, and O. Pierre-Louis, Phys. Rev. Lett. **106**, 195501 (2011).
[31] S. Stoyanov, Japan. J. Appl. Phys. **30**, 1 (1991).
[32] C. Misbah, O. Pierre-Louis, and Y. Saito, Rev. Mod. Phys. **82**, 981 (2010).